RSC Advances

PAPER

View Article Online
View Journal | View Issue

Cite this: *RSC Adv.*, 2025, **15**, 23845

Multifunctional carbon dots from *Polygonatum kingianum* and *Gastrodia elata*: synthesis, characterization, and biomedical applications

Shengting Zhang,[b] Huili Tao,[a] Xiaodan Zheng,[c] Sha Zhao[d] and Yunlin Wei*[e]

Received 4th May 2025
Accepted 20th June 2025

DOI: 10.1039/d5ra03140k

rsc.li/rsc-advances

Carbon dots (CDs) derived from *Polygonatum kingianum* (Pk-CDs) and *Gastrodia elata* (Ge-CDs) were synthesized *via* a one-step hydrothermal method and characterized using TEM, XPS, and FTIR. Pk-CDs and Ge-CDs exhibited uniform spherical morphologies (6.2 ± 0.3 nm and 6.8 ± 0.4 nm, respectively) and excitation-dependent fluorescence. Antibacterial assays demonstrated potent inhibition against Gram-positive (*S. aureus*, *B. cereus*) and Gram-negative bacteria (*E. coli*, *P. aeruginosa*). *In vitro* antioxidant assays demonstrated that Pk-CDs outperformed Ge-CDs in DPPH radical and superoxide anion scavenging, with IC_{50} values of 2.994 mg mL^{-1} and 0.30 mg mL^{-1}, respectively. *In vivo* studies in a D-galactose-induced oxidative stress model confirmed significant improvements in SOD, GSH-Px, and MDA levels. These findings highlight the multifunctional properties of Pk-CDs and Ge-CDs, and underscore their potential as natural product-derived nanomaterials for biomedical applications, particularly as antibacterial and antioxidant agents.

1. Introduction

Carbon dots (CDs) have garnered significant interest in recent years due to their unique optical properties, simple synthesis, and versatile applications in fields such as bioimaging, sensors, drug delivery, and catalysis.[1–11] Derived from various carbon sources, CDs exhibit excellent water solubility, chemical stability, and low cytotoxicity.[12] Among these, carbon dots synthesized from natural products, particularly traditional Chinese medicines (TCM), have emerged as a promising area of research due to their potential biological activities. In this study, it specifically refers to Pk-CDs (from *Polygonatum kingianum*) and Ge-CDs (from *Gastrodia elata*).

Polygonatum kingianum (Pk) and *Gastrodia elata* (Ge) are two significant TCM components known for their various pharmacological properties. Pk, commonly referred to as "Huángjīng", is traditionally used for enhancing immune function, anti-aging, and neuroprotection.[13–16] Ge, known as "Tiānmá", is revered for its usage in treating headaches, dizziness, convulsions, and neurodegenerative diseases.[17–19] Despite their wide utilization in TCM, the incorporation of these herbs into next-generation nanomaterials, such as carbon dots, is relatively nascent and requires comprehensive exploration.

In this study, two kinds of TCM carbon dots (Pk-CDs and Ge-CDs) were prepared from Pk and Ge using the hydrothermal method.[20] The structure and optical properties of the prepared TCM-CDs were analyzed by transmission electron microscopy (TEM), X-ray photoelectron spectroscopy (XPS), Fourier-transform infrared spectroscopy (FT-IR), and ultraviolet-visible spectroscopy (UV-vis), and so on. The structural and optical properties of the prepared TCM-CDs were analyzed. The biological activities of Pk-CDs and Ge-CDs were explored in terms of both bacteriostatic and antioxidant activities. The Oxford cup method was used to demonstrate the inhibitory effect of the two TCM-CDs on both Gram-negative and Gram-positive bacteria. The morphological changes of the bacteria were detected by scanning electron microscopy (SEM), and finally, the expression of relevant genes of the strains co-cultured with the two TCM-CDs was determined by qPCR.

Antibacterial resistance stands as a global health challenge necessitating novel therapeutic solutions.[21] In this context, carbon-based nanomaterials have shown promise due to their inherent antimicrobial properties. This research delves into the antibacterial efficacy of Pk-CDs and Ge-CDs against both Gram-positive and Gram-negative bacteria. By analyzing minimum inhibitory concentrations (MIC), bacterial growth curves, and morphological changes, this study elucidates the potential mechanisms underpinning the antibacterial actions of these CDs.

Furthermore, oxidative stress is implicated in various pathological states, including aging and chronic diseases.[22]

[a]*School of Ethnic Medicine, Yunnan Minzu University, Kunming, 650500, China*
[b]*School of Ethnic Medicine, Yunnan Minzu University, Kunming, 650500, China*
[c]*Faculty of Life Science and Technology, Kunming University of Science and Technology, Kunming, 650500, China*
[d]*School of Ethnic Medicine, Yunnan Minzu University, Kunming, 650500, China*
[e]*Faculty of Life Science and Technology, Kunming University of Science and Technology, Kunming, 650500, China. E-mail: weiyunlin@kust.edu.cn*

Antioxidants derived from natural sources continue to be pivotal in mitigating oxidative damage.[23] Here, the antioxidant capacities of Pk-CDs and Ge-CDs were assessed through *in vitro* assays, such as DPPH radical scavenging and total reducing power, along with *in vivo* studies using a D-galactose-induced oxidative damage mouse model to examine the TCM-CDs' efficacy in combating oxidative stress.

In summary, this study aims to develop a comprehensive understanding of the synthesis, characterization, and multifaceted biological activities of Pk-CDs and Ge-CDs. By leveraging the pharmacological potential of TCM ingredients, this research intends to pave the way for novel applications of carbon dots in antimicrobial and antioxidative therapies.

2. Materials and methods

2.1 Preparation and characterization of carbon dots from Pk and Ge

2.1.1 Materials and reagents. Pk (purity = 90%) and Ge (purity = 90%) were purchased from Xirang Technology Co., Ltd (Yunnan, China). Diammonium hydrogen phosphate (purity: premium pure) and ethylenediamine (EDA, purity = 1.0 mg mL^{-1}) were obtained from Aladdin Biochemical Technology Co., Ltd (Shanghai, China). Citric acid (purity = ≥99.5%), disodium hydrogen phosphate (Na_2HPO_4, purity = 99.95%), and sodium hydroxide (NaOH, purity = ≥97.0% M) were purchased from Tianjin Zhiyuan Chemical Reagent Co., Ltd (Tianjin, China). Ultrapure water (18.2 MΩ cm, 25 °C) was prepared using a Milli-Q system.

2.1.2 Synthesis of Pk-CDs, Ge-CDs, N,P-CQDs, and N,F-CQDs. Carbon dots (CDs) were synthesized from Pk and Ge separately using a one-step hydrothermal method. Briefly, each plant material was pulverized into a fine powder using a mechanical grinder. One gram of the resulting powder was mixed with 20 mL of deionized water and ultrasonicated for 15 minutes to ensure complete dispersion. The mixture was then transferred into a polytetrafluoroethylene-lined autoclave and heated at 180 °C for 12 hours. After naturally cooling to room temperature, the resulting solution was centrifuged at 13 000 × *g* for 15 minutes to remove large particulates and insoluble residues. The supernatant was subsequently filtered through a 0.22 μm membrane to remove any remaining debris. To ensure the removal of small molecular wright by-products and residual plant metabolites (*e.g.*, sugars, flavonoids, amino acids), the filtered solution was subjected to dialysis (molecular weight cut-off: 1000 Da) against deionized water for 48 hours, with water replaced every 8 hours. The purified CD solution was then vacuum freeze-dried to obtain Pk-CDs and Ge-CDs in powder form. The powders were stored at 4 °C until further use. No mixture synthesis of Pk and Ge was performed; the two types of CDs were synthesized and analyzed independently to compare their respective physicochemical and biological properties.

In addition, nitrogen and phosphorus co-doped carbon quantum dots (N,P-CQDs) and nitrogen and fluorine co-doped carbon quantum dots (N,F-CQDs) were synthesized using the same hydrothermal procedure with appropriate precursors containing nitrogen, phosphorus, and fluorine sources. Briefly, 1 g of precursor powder was dissolved in 20 mL of deionized water, transferred to a polytetrafluoroethylene-lined autoclave, and heated at 180 °C for 12 hours. The product was then centrifuged at 13 000 × *g* for 15 minutes, filtered through a 0.22 μm membrane, vacuum-dried, and stored at 4 °C for subsequent experiments.

2.1.3 Purification strategy of CDs. In the present study, a combination of centrifugation and dialysis was employed to purify the carbon dots and effectively eliminate unreacted plant metabolites and small-molecule by-products. While centrifugation efficiently removes insoluble residues and large particulates, dialysis is essential for removing water-soluble impurities. Compared to column chromatography, dialysis is more practical for bulk preparation of water-dispersible CDs, avoiding organic solvent contamination and sample loss. However, dialysis is time-consuming and has limited efficiency in removing high-molecular-weight impurities. Future studies may consider integrating methods such as HPLC or membrane filtration to further improve purification efficiency and scalability.

2.1.4 Characterization of the structure and optical properties of Pk-CDs and Ge-CDs. The structure and optical properties of Pk-CDs and Ge-CDs were characterized using various techniques. TEM (JEOL2100F, FEI, Holland)was used to analyze the spacing, particle size, shape, and crystal structure of the CDs. X-ray photoelectron spectroscopy (XPS) (Thermo Scientific K-Alpha, Thermo Fisher Scientific Inc. U.S.A.) was employed to analyze the elemental composition, chemical bond content, and surface functional groups of the CDs. Fourier-transform infrared spectroscopy (FTIR) (Thermo Fisher Nicolet Is10, German)was used to infer the surface chemical functional group structure and chemical composition of the CDs.

The UV-visible (UV-vis) (UV-2600, Shimadzu, Japan) spectra were analyzed to study the ultraviolet absorption characteristics, absorbance, and structural transitions of the CDs. The fluorescence emission spectra were measured by fluorescence spectrophotometry (G9800A, Shimadzu, Japan) by subjecting the aqueous solution of the CDs to full-scan fluorescence emission under excitation wavelength until the fluorescence was undetectable, thereby determining the optimal excitation wavelength with the highest fluorescence intensity.

2.1.5 Sample preparation for characterization. Prior to characterization, all CD samples – including Pk-CDs, Ge-CDs, N,P-CQDs, and N,F-CQDs – were carefully prepared to ensure accuracy and reproducibility of measurements. For TEM, a small amount of each CD powder was redispersed in deionized water to form a 0.5 mg mL^{-1} aqueous solution. The solution was sonicated for 10 minutes to ensure uniform dispersion and then a droplet was deposited onto a carbon-coated copper grid, followed by drying at room temperature under ambient conditions.

For XPS and FTIR, the freeze-dried CD powders were directly used without further modification. Prior to XPS analysis, samples were pressed into thin, uniform pellets and affixed onto conductive adhesive tape. For FTIR, approximately 1 mg of CD powder was thoroughly mixed with 100 mg of dried KBr and pressed into a transparent disc using a hydraulic press.

UV-vis and fluorescence spectroscopic measurements were conducted using freshly prepared CD aqueous solutions at a concentration of 0.1 mg mL^{-1}. These solutions were filtered through a 0.22 μm membrane to eliminate potential particulate interference before analysis. All measurements were performed at room temperature using quartz cuvettes with a 1 cm path length. Each sample was analyzed in triplicate to ensure consistency and reliability of the spectral data.

2.2 Biological activity of Pk-CDs and Ge-CDs

2.2.1 Antibacterial activity. *Escherichia coli* BW25113 (*E. coli*), *Pseudomonas aeruginosa* ATCC 10145 (*P. aeruginosa*), *Staphylococcus aureus* ATCC 25923 (*S. aureus*), and *Bacillus cereus* MYB41-22 (*B. cereus*) were inoculated at 2% inoculum into 5 mL of Luria–Bertani broth (LB) liquid medium respectively, and shaken at 37 °C until the optical density (OD) at 600 nm was approximately 0.5.

2.2.2 Determination of the antibacterial activity of carbon dots by Oxford cup method. Sterilized Oxford cups (outer diameter: 8 mm, inner diameter: 6 mm, height: 10 mm) were placed on LB agar plates pre-inoculated with bacterial suspensions (*E. coli*, *P. aeruginosa*, *S. aureus*, and *B. cereus*; OD600 ≈ 0.5). A sterile pipette was used to inject 50 μL of TCM-CDs solutions of 6.25, 12.5, 25, 50, and 100 mg mL^{-1} into each Oxford cup. Sterile water was used as a negative control, while gentamicin (10 μg mL^{-1}) served as the positive control for *E. coli* and *P. aeruginosa*, and ampicillin (10 μg mL^{-1}) was used for *S. aureus* and *B. cereus*. The plates were incubated at 37 °C for 24 hours. Each concentration was tested in triplicate, and antibacterial activity was evaluated by measuring the diameter of the inhibition zones.

2.2.3 Determination of minimum inhibitory concentration (MIC). Each 1 mL of filtered CDs solution was added to 9 mL of LB solid medium melted at approximately 55 °C to adjust the final concentration to 100, 50, 25, 12.5, 6.25 mg mL^{-1}. After solidification, 100 μL of the prepared bacterial suspension was evenly spread. The plates were incubated at 37 °C for 24 hours, and the lowest concentration that completely inhibited bacterial growth was recorded as the MIC.

2.2.4 MTT assay. Log-phase cells (Courtesy of Molecular Medicine Research Center, School of Life Science and Technology, Kunming University of Science and Technology HeLa and HaCa) were harvested using trypsin digestion, and the cell density was adjusted to 0.5805×10^5 cells per mL. The cells were then seeded into 96-well plates and incubated at 37 °C in a humidified incubator with 5% CO_2 for 24 hours to allow for cell attachment. After 24 hours, 40 μL of Ge-CDs or Pk-CDs diluted in culture medium at concentrations ranging from 10 mg L^{-1} to 60 mg L^{-1} was added to each well, followed by another 24 hour incubation under the same conditions. Subsequently, 20 μL of MTT solution was added to each well, and the cells were incubated for an additional 4 hours at 37 °C. The culture medium was then carefully removed, and 150 μL of DMSO was added to each well to dissolve the formazan crystals, followed by 2 minutes of shaking. Finally, the absorbance was measured at 492 nm using a microplate reader to assess cell viability.

2.2.5 Bacterial growth curve determination. *E. coli*, *P. aeruginosa*, *S. aureus*, and *B. cereus* were inoculated at 2% inoculum into 100 mL of LB liquid medium. One set was untreated as control, and other three sets were treated with CDs at 1/2 MIC, MIC, and 2 MIC concentrations respectively. The initial OD600 was recorded as the zero-time point. The cultures were incubated at 37 °C, 150 rpm, and OD600 was measured every 2 hours for a total of 8 hours. Growth curves were plotted with incubation time as the *x*-axis and OD600 value as the *y*-axis.

2.2.6 Extraction of total RNA from bacteria. *E. coli*, *P. aeruginosa*, *S. aureus*, and *B. cereus* were inoculated at 2% inoculum into 5 mL of LB medium, and cultured at 37 °C, 150 rpm until OD600 reached 0.6. The cultures were divided into three groups: one untreated control and two treated with CDs at 1/2 MIC. Culturing was continued for 1 hour. Each 1 mL of bacterial suspension was centrifuged at 13 000 rpm at room temperature for 1 minute, the supernatant was discarded, and the pellet was rapidly frozen with liquid nitrogen and stored at −80 °C. Total RNA was extracted using the kit according to the manufacturer's protocol (Tiangen Biochemical Technology Co., Ltd).

2.2.7 cDNA synthesis. Reverse transcription was performed using the TIANGEN FastKing RT Kit (with gDNase) according to the manufacturer's instructions.

2.2.8 RT-PCR for gene expression analysis. In this experiment, the changes in the expression of selected genes in *E. coli* and *S. aureus* after the addition of two types of carbon quantum dots (N,P-CQDs and N,F-CQDs) were investigated. These CQDs are chemically synthesized and differ from the Pk-CDs and Ge-CDs, which are biologically derived from TCM sources Pk and Ge, respectively. The expression of the genes in the control bacteria without the addition of CQDs was used as a reference to compare and analyze the obtained RT-PCR data with the data of the reference genes, and the 2-ΔΔ*C*t method was chosen to process the RT-PCR data in the experiment.

2.3 Antioxidant activity

2.3.1 *In vitro* antioxidant activity

2.3.1.1 DPPH radical scavenging assay. The method was modified from Pyrzynska *et al.*[24]'s study. Gradient concentrations of TCM-CDs in ethanol, 0.1 mmol L^{-1} DPPH ethanol solution, and 50 mmol L^{-1} Tris–HCl buffer were prepared. Sample mixtures contained 200 μL of test sample, 4 mL of DPPH solution, and 450 μL of Tris–HCl buffer. Control mixtures contained 200 μL of test sample, 4 mL of absolute ethanol, and 450 μL of Tris–HCl buffer. Blank mixtures contained 200 μL of ethanol, 4 mL of DPPH solution, and 450 μL of Tris–HCl buffer. Mixtures were incubated at room temperature in the dark for 30 minutes. Absorbance was measured at 517 nm using a 1 cm quartz cuvette, and the DPPH radical scavenging rate was calculated as:

$$\text{DPPH radical scavenging rate (\%)} = \left[1 - \frac{A_{\text{sample}} - A_{\text{compare}}}{A_{\text{blank}}}\right] \times 100 \quad (1)$$

where: A_{sample} = absorbance of the sample mixture with TCM-CDs and DPPH.A_{compare} = absorbance of the blank mixture

with DPPH but no TCM-CDs.A_{blank} = absorbance of the blank mixture with DPPH but no TCM-CDs.

2.3.1.2 Superoxide anion radical scavenging assay. This method was modified from Zhang *et al.*[25] The nicotinamide adenine dinucleotide (NADH)/phenazine methosulfate (PMS)/nitroblue tetrazolium (NBT) system was used to measure the superoxide anion ($O_2^{-\bullet}$) scavenging capacity. PMS solution, 468 mM NADH solution, and 150 mM NBT solution were prepared using phosphate buffer solution (PBS, 0.1 M, pH = 7.4) at concentrations of PMS, 468 mM NADH solution and 150 mM NBT solution, respectively, and stored away from light. The TCM-CDs were prepared into a gradient concentration of ethanol solution, and the absorbance value at 560 nm was measured after standing at room temperature for 5 min. The superoxide anion radical scavenging rate was calculated using the formula as follows:

$$\text{Superoxide scavenging rate (\%)} = \left[1 - \frac{A_{sample} - A_{compare}}{A_{blank}}\right] \times 100 \quad (2)$$

whereA_{sample} = absorbance of the reaction mixture with TCM-CDs and all reagents. $A_{compare}$ = absorbance of the mixture with TCM-CDs but without PMS. A_{blank} = absorbance of the mixture with all reagents but no TCM-CDs.

2.3.1.3 Hydroxyl radical scavenging assay. Referring to the method of Chen and Huang[26] with slight modification, the specific method was as follows: 1.5 mmol L^{-1} ferrous sulfate solution, 20 mmol L^{-1} sodium salicylate solution, 6 mmol L^{-1} H_2O_2 solution were configured, ready to use, and stored away from light. TCM-CDs ethanol solutions of different concentrations were incubated at 37 °C for 1 hour in a water bath. Absorbance at 562 nm was measured, and the hydroxyl radical scavenging rate was calculated as:

$$\text{Hydroxyl scavenging rate (\%)} = \left[1 - \frac{A_{sample} - A_{compare}}{A_{blank}}\right] \times 100 \quad (3)$$

where A_{sample} = absorbance of the full reaction mixture including TCM-CDs.$A_{compare}$ = absorbance without sodium salicylate (control).A_{blank} = absorbance of the reaction mixture without TCM-CDs.

2.3.1.4 Ferrous ion chelating ability. Referring to Jiao's method[27] with slight improvement, the specific experimental method was as follows: 5 mmol L^{-1} phenanthrozine solution and 200 mmol L^{-1} $FeCl_2$ solution were configured. Take 1 mL of ethanol solution of TCM-CDs with different concentration gradients, add 0.5 mL of 200 mmol L^{-1} $FeCl_2$ solution, mix well, add 1 mL of 5 mmol L^{-1} phenanthrozine solution to start the reaction, and continue to add 1 mL of anhydrous ethanol, vibrate vigorously to mix well and then stand for 10 min, and then determine its absorbance value at 562 nm. The chelating rate was calculated as:

$$\text{Chelating rate (\%)} = \left[1 - \frac{A_{sample} - A_{compare}}{A_{blank}}\right] \times 100 \quad (4)$$

whereA_{sample} = absorbance of the reaction mixture containing TCM-CDs.$A_{compare}$ = absorbance of the mixture without phenanthrozine.A_{blank} = absorbance of the mixture without TCM-CDs.

2.3.1.5 Ferric ion reducing ability. The reduction capacity of the two selected TCM-CDs for Fe^{3+} was determined with reference to Lue's method.[28] TCM-CDs ethanol solutions (1 mL) were mixed with 2.5 mL of 0.2 M PBS buffer (pH 6.6) and 2.5 mL of 30 mM $K_3Fe(CN)_6$ solution. Mixtures were incubated at 50 °C for 20 minutes, followed by addition of 2.5 mL of 0.6 M (molarity = mol L^{-1}) trichloroacetic acid to terminate the reaction. After centrifugation at 850 × *g* for 10 minutes, 2 mL of supernatant was mixed with 2 mL of distilled water and 0.4 mL of 4 mmol L^{-1} $FeCl_3$ solution. After standing for 10 min, absorbance at 700 nm was measured. Higher absorbance indicates greater reducing ability.

2.3.1.6 Total antioxidant capacity. With reference to the phosphomolybdenum complex method of Qinghao Shi.[29] TCM-CDs ethanol solutions (0.4 mL) were mixed with 4 mL of phosphomolybdenum reagent (final concentrations: sulfuric acid, 0.6 M; sodium phosphate, 28 mM; ammonium molybdate, 4 mM) and incubated at 95 °C for 90 minutes. After cooling to room temperature, absorbance at 695 nm was measured. Higher absorbance indicates stronger antioxidant capacity.

2.3.2 *In vivo* antioxidant activity. Firstly, the D-galactose-induced oxidative damage model in mice was established (divided into 9 groups, as in Table 1), and then by observing the growth and mental status of mice during the experimental period, such as activity, hair color, urination and defecation, how much they eat or drink, and their mental status. Finally, SOD, GSH-Px and MDA were measured in serum and tissues (heart, liver and kidney) of mice.

2.4 Biofilm inhibition experiments

The biofilm inhibition efficacy of Pk-CDs and Ge-CDs against two bacterial strains was evaluated using a 96-well plate crystal violet (CV) staining method. Single colonies were inoculated into LB broth and cultured overnight in a shaking incubator (*Pseudomonas* sp. strain 41–22 at 28 °C, 180 rpm; *Escherichia coli* at 37 °C, 180 rpm). Upon reaching the exponential growth

Table 1 Grouping of mice model of oxidative damage induced by D-gal[a]

Group	Inject a drug	
1	Normal control group (NG, physiological saline)	
2	D-Galactose oxidative damage model control group (model group, physiological saline)	
3	Positive control group (PG, L-AA mg per kg bw per d)	
4	Pk-CDs	Low dose group (LD, 400 mg per kg bw·per d)
5		Middle dose (MD, 200 mg per kg bw·per d)
6		High dose group (HD, 100 mg per kg bw·per d)
7	Ge-CDs	Low dose group (LD, 400 mg per kg bw·per d)
8		Middle dose (MD, 200 mg per kg bw·per d)
9		High dose group (HD, 100 mg per kg bw·per d)

[a] L-AA = L-ascorbic acid, PG = positive control group, LD = low does, MD = middle dose, HD = high dose, MG = model group, Pk-CDs = *Polygonatum kingianum*-carbon dots, Ge-CDs = *Gastrodia elata*-carbon dots.

phase, bacterial cultures were diluted 1 : 100 in fresh LB medium and set aside for subsequent use. CD solutions were diluted in LB broth to final concentrations of 25, 50, and 100 mg L^{-1}. Then, 100 μL of each diluted bacterial suspension was added to individual wells of a 96-well plate, followed by 100 μL of the CD solutions (resulting in final concentrations of 12.5, 25, and 50 μg mL^{-1}). Plates were sealed with parafilm and incubated under static conditions for 36 h (28 °C for *Pseudomonas*, 37 °C for *E. coli*). After incubation, the culture medium was removed, and wells were washed five times with 200 μL of PBS. The attached biofilms were fixed with methanol for 15 min, followed by staining with 100 μL of 1% (w/v) crystal violet for 10 min under shaking to ensure uniform dye penetration. The excess stain was carefully aspirated, and the wells were rinsed with running water. After air-drying, 100 μL of 33% glacial acetic acid was added to each well and incubated at 37 °C for 30 min to solubilize the bound dye. The absorbance was measured at 595 nm using a microplate reader. Each treatment was performed in triplicate. Biofilm formation (%) was expressed as the mean absorbance of replicate wells, and the biofilm inhibition rate (%) was calculated as follows:

$$\text{Biofilm inhibition rate (\%)} = 100 - \text{biofilm formation (\%)}.$$

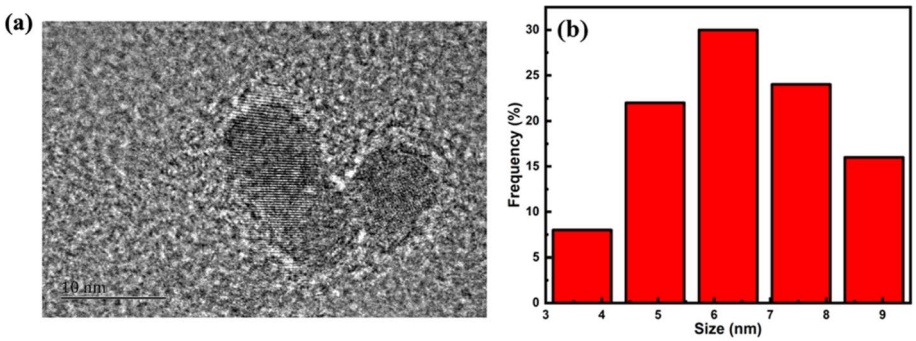

Fig. 1 (a) TEM image of Pk-CDs; (b) interplanar spacing of Pk-CDs.

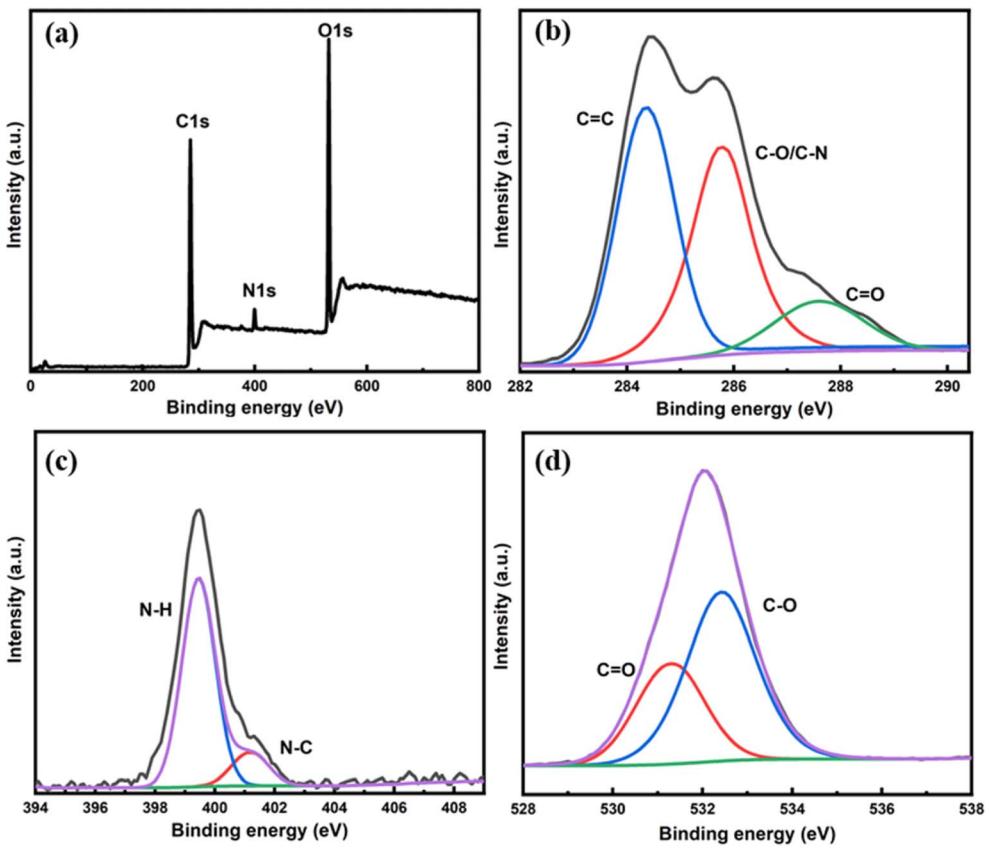

Fig. 2 (a) XPS spectra of Pk-CDs; (b) high resolution C 1s spectrogram; (c) high resolution N 1s spectrogram; (d) high resolution O 1s spectrogram.

3. Results

3.1 Characterization of Pk-CDs and Ge-CDs

3.1.1 Structural characterization of Pk-CDs and Ge-CDs. TEM images (Fig. 1a and 5a) revealed that both Pk-CDs and Ge-CDs were spherical carbon nanoparticles, uniformly dispersed without aggregation. The particle size ranged from 3 to 10 nm, with average diameters of 6.2 ± 0.3 nm for Pk-CDs (Fig. 1b) and 6.8 ± 0.4 nm for Ge-CDs (Fig. 5b). High-resolution TEM images showed a interplanar spacing of 0.21 nm for both Pk-CDs and Ge-CDs, indicative of graphitic domains.

XPS analysis confirmed the presence of carbon, nitrogen, and oxygen in both samples. For Pk-CDs, characteristic peaks appeared at C 1s: 280.6 eV, N 1s: 402.8 eV, and O 1s: 534.7 eV (Fig. 2a), while for Ge-CDs, these were C 1s: 285.6 eV, N 1s: 401.9 eV, and O 1s: 535.5 eV (Fig. 6a). High-resolution C1s spectra for both CDs displayed peaks corresponding to C=C, C–O/C–N, and C=O structures (Pk-CDs: 284.36 eV, 285.75 eV, 287.60 eV; Ge-CDs: 284.2 eV, 286.1 eV, and 288.0 eV) (Fig. 2b and 6b). The N 1s spectra showed peaks around 399.8–400.8 eV (Pk-CDs: N–H at 399.85 eV, N–C at 400.84 eV; Ge-CDs: N–H at 399.45 eV, N–C at 400.04 eV), associated with C–N–H and N–C bonds (Fig. 2c and 6c). Similarly, the O 1s spectra revealed peaks at 531–533 eV (Pk-CDs: C=O at 531.16 eV, C–O at 532.82 eV; Ge-CDs: C=O at 531.86 eV, C–O at 533.0 eV), indicating the presence of C=O and C–O groups, respectively (Fig. 2d and 6d).

FTIR spectra further confirmed the presence of functional groups (Fig. 3 and 7). Both Pk-CDs and Ge-CDs exhibited similar characteristic peaks, including the O–H stretching vibration, $-CH_2$ stretching peak, C=O bending vibration, C–O–C stretching vibrations, and N–H stretching vibration. Specifically, the O–H stretching vibration was observed at 3386.06 cm^{-1}, corresponding to hydroxyl, amine, or carboxyl groups. The $-CH_2$ stretching peak appeared at 2933.49 cm^{-1}, while the C=O bending vibration was detected at 1663.33 cm^{-1}. C–O–C stretching vibrations were evident at 1077.07 cm^{-1} and 1030.58 cm^{-1}, and the N–H stretching vibration was noted at 771.50 cm^{-1}. These FTIR results were consistent with XPS data, confirming the abundance of hydrophilic functional groups, which contribute to the excellent water solubility of both types of CDs.

3.1.2 Optical characterization of Pk-CDs and Ge-CDs. The UV-vis absorption spectra of both Pk-CDs and Ge-CDs exhibited a characteristic peak at 280 nm (Fig. 4a and 8a). The maximum excitation wavelength (Ex) for 329 nm for Pk-CDs and 328 nm for Ge-CDs, with a corresponding emission wavelength of 419 nm and 429 nm, respectively (Fig. 4a and 8a). The emission spectrum at this Ex exhibited strong fluorescence intensity with broad, slightly symmetrical profiles. When the excitation wavelength was gradually adjusted from 300 nm to 400 nm, the emission spectra of both Pk-CDs and Ge-CDs showed a red shift, indicating pronounced excitation-dependent fluorescence behavior (Fig. 4b and 8b). Optical assays were performed using a CD concentration of 0.1 mg mL^{-1}. To assess fluorescence stability, a series of dilutions ranging from 0.01 to 0.5 mg mL^{-1} was tested, and no significant fluorescence quenching was observed across this concentration range.

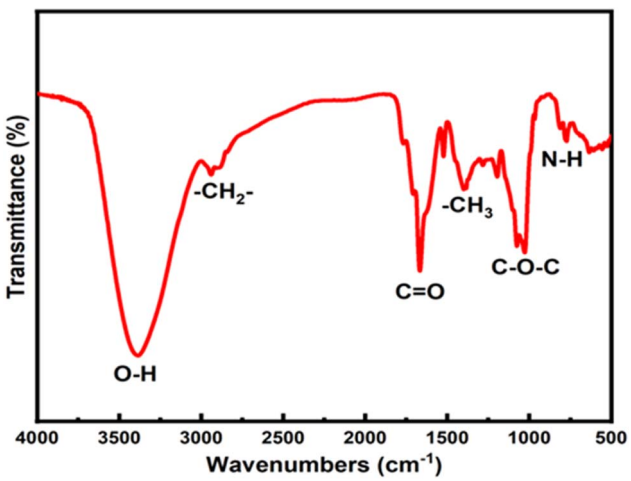

Fig. 3 Infrared spectrogram of Pk-CDs.

3.2 Antibacterial activity studies

3.2.1 Antibacterial activity. Using the Oxford cup method, it was observed that both Pk-CDs and Ge-CDs inhibited the

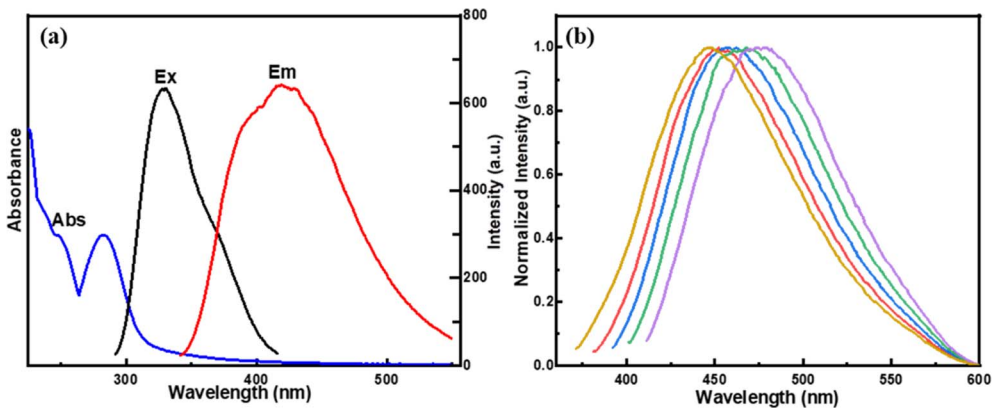

Fig. 4 (a) Absorption spectrum (Abs, blue), excitation spectrum (Ex, black), and emission spectrum (Em, red) plots; (b) normalized intensity curve with wavelength variation.

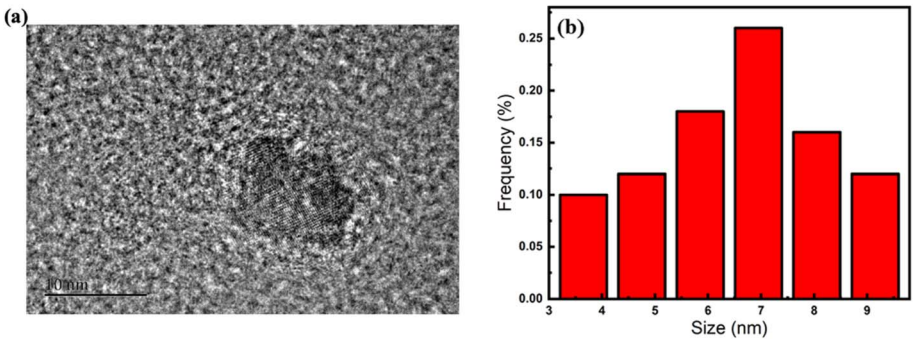

Fig. 5 (a) TEM image of Ge-CDs; (b) interplanar spacing of Ge-CDs.

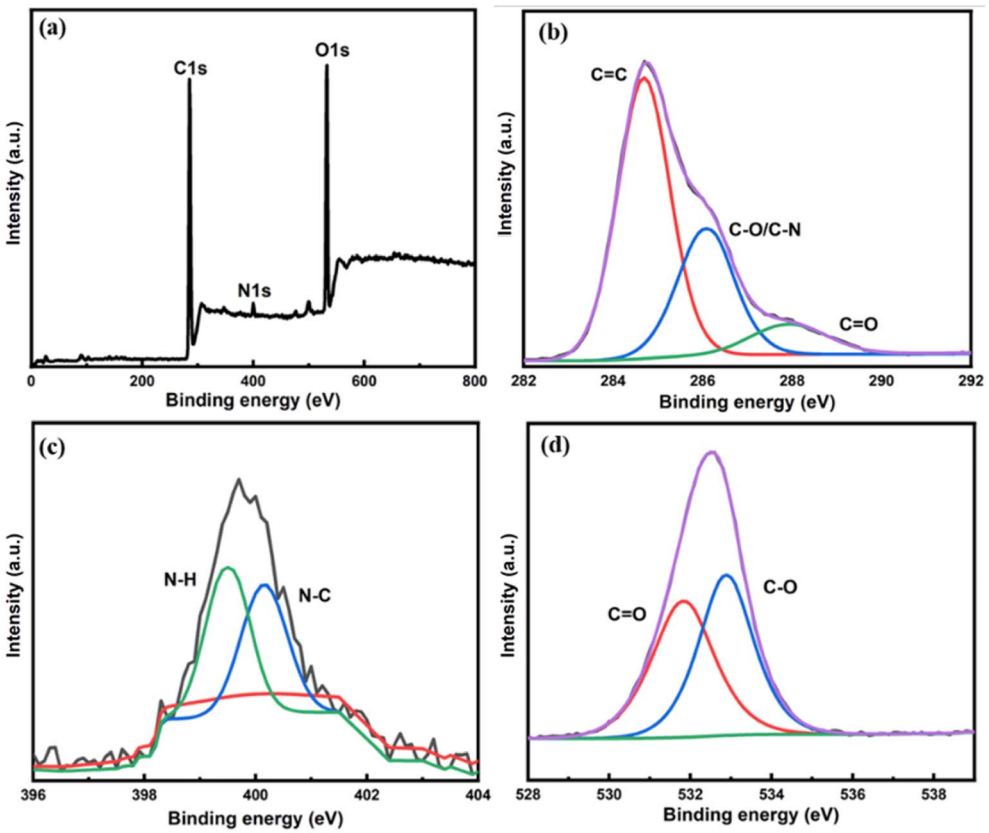

Fig. 6 (a) XPS spectra of Ge-CDs; (b) high resolution C 1s spectrogram; (c) high resolution N 1s spectrogram; (d) high resolution O 1s spectrogram.

growth of two Gram-negative bacteria (*E. coli* and *P. aeruginosa*) and two Gram-positive bacteria (*S. aureus* and *B. cereus*). The inhibition effect was ranked as Pk-CDs > Ge-CDs (Fig. 9, Tables 2 and 3). In addition, a comparison by bacterial classification shows that the two herbal CDs had the best inhibitory effect on the Gram-positive bacterium *B. cereus*, followed by the Gram-negative bacterium *P. aeruginosa*, with a slightly weaker inhibitory effect on another Gram-positive bacterium *S. aureus* and another Gram-negative bacterium and *E. coli*, and there was no difference in the inhibitory effect between Gram-negative bacteria and Gram-positive bacteria. As shown in Table 2, the minimum inhibitory concentrations (MIC) of Pk-CDs and Ge-CDs were 25 mg mL^{-1} and 50 mg mL^{-1} for *E. coli*, respectively; 6.25 mg mL^{-1} and 12.5 mg mL^{-1} for *P. aeruginosa*; 25 mg mL^{-1} for *S. aureus*; and 6.25 mg mL^{-1} and 12.5 mg mL^{-1} for *B. cereus*. This indicated that Pk-CDs had the best inhibition effect on *B. cereus* and *P. aeruginosa*.

3.2.2 Bacterial growth curves. The inhibitory effect of different concentrations of TCM-CDs on bacterial growth varied. With increasing concentrations of TCM-CDs, the inhibitory effect became more pronounced. TCM-CDs showed

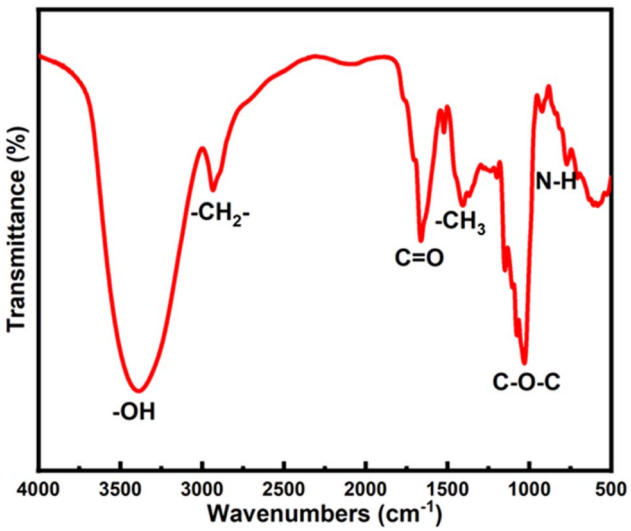

Fig. 7 Infrared spectrogram of Ge-CDs.

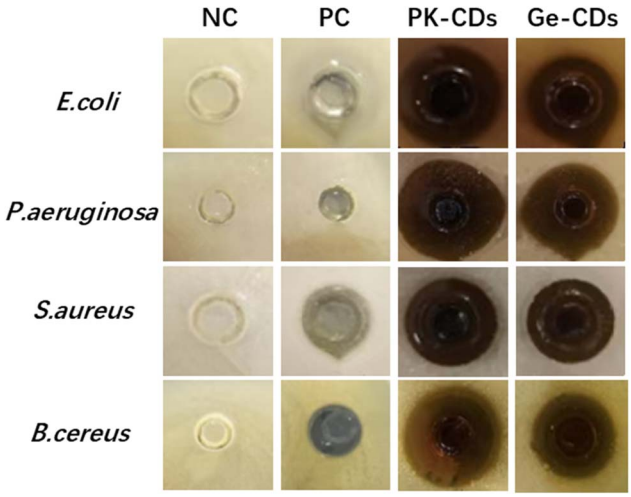

Fig. 9 Antibacterial circle diagram, showing the antibacterial activity of different samples against different bacteria.

similar concentration-dependent antibacterial effects (Fig. 10 and 11).

3.2.3 Cell viability. The effects of different concentrations of Ge-CDs and Pk-CDs on the viability of HeLa and HaCaT cells were evaluated. As shown in the figure (a: HeLa, b: HaCaT), both Ge-CDs and Pk-CDs exhibited low cytotoxicity toward the two cell lines, with cell viability remaining above 80%. These results preliminarily indicate that Ge-CDs and Pk-CDs possess low toxicity (Fig. 12).

3.2.4 Bacterial morphological changes. Scanning electron microscopy (SEM) images (Fig. 13) showed that untreated *E. coli*, *P. aeruginosa*, *S. aureus*, and *B. cereus* had intact cell membrane structures with good adhesion between the cells. After treatment with TCM-CDs, significant changes were observed in all bacteria. The cell membranes and biofilms were severely damaged, most cells no longer had intact structures, and intracellular substances leaked out.

3.2.5 Changes in bacterial gene expression. qPCR analysis revealed significant changes in gene expression after co-culture with TCM-CDs for 1 hour ($p < 0.01$). As shown in Fig. 14(a) and (b), the expression of the waaC gene was significantly reduced. The sgtB gene expression was also markedly decreased, indicating an impact on the cell membrane synthesis of *E. coli*, *P. aeruginosa*, *S. aureus*, and *B. cereus*, consistent with the SEM results (Fig. 14(c) and (d)).

qPCR results showed that the expression of the polA gene, which regulates DNA replication in bacteria, was significantly inhibited after treatment with the two TCM-CDs. This suggested that TCM-CDs could effectively inhibit DNA replication in bacteria. Furthermore, the expression of the ptsI gene was significantly suppressed by the two TCM-CDs, affecting the bacterial phosphotransferase system (PTS) and reducing glucose transport through the PTS pathway, thereby inhibiting bacterial growth and metabolism.

As shown in Fig. 14, neither TCM-CD significantly affected the expression of rpoA and rpoB genes, which regulate genetic information expression in *E. coli*, *P. aeruginosa*, *S. aureus*, and *B. cereus*. Additionally, the expression of the ftsA gene, which regulates cell division, was significantly suppressed by both

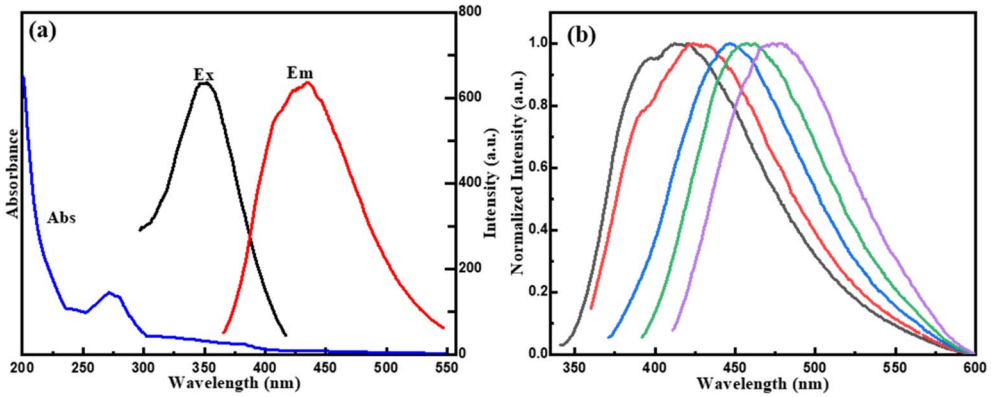

Fig. 8 (a) Absorption spectrum (Abs, blue), excitation spectrum (Ex, black), and emission spectrum (Em, red) plots; (b) normalized intensity curve with wavelength variation.

Table 2 Diameters of inhibition zone of two TCM-CDs against four bacteria

	Zone of inhibition in diameter/(cm)					
			Pk-CDs (g mL^{-1})		Ge-CDs (g mL^{-1})	
Microbe	Negative control	Positive control	1	0.5	1	0.5
E. coli	—	1.40 ± 1.16	1.85 ± 0.98	0.78 ± 0.45	1.6 ± 0.78	0
P. aeruginosa	—	0.82 ± 0.64	2.56 ± 0.83	0.90 ± 0.75	2.3 ± 0.72	0.82 ± 0.47
S. aureus	—	0.95 ± 0.54	1.60 ± 0.80	0.82 ± 0.45	1.4 ± 0.85	0
B. cereus	—	1.18 ± 0.54	>30.00	2.13 ± 0.53	>30.00	1.88 ± 0.52

Table 3 Minimum inhibitory concentration of two TCM-CDs

	MIC (mg mL^{-1})	
Strain	Pk-CDs	Ge-CDs
E. coli	25	50
P. aeruginosa	6.25	12.5
S. aureus	25	25
B. cereus	6.25	12.5

TCM-CDs, effectively hindering bacterial binary fissions, thus exhibiting strong antibacterial action. These results were consistent with the bacterial growth curve experiments.

3.3 Antioxidant activity

3.3.1 *In vitro* antioxidant activity. The scavenging activities of different concentrations of TCM-CDs solutions on DPPH radicals were different, and the scavenging rate of DPPH radicals showed a tendency of increasing and then stabilizing with the increase of the concentrations of two kinds of TCM-CDs, which showed an obvious quantitative-effect relationship. The concentrations of the two TCM-CDs at 50% scavenging rate were, in descending order, L-ascorbic acid (L-AA) (0.1314 mg mL^{-1}) < Pk-CDs (2.994 mg mL^{-1}) < Ge-CDs (14.33 mg mL^{-1}). With the increase of concentration, the scavenging rate of Pk-CDs increased and leveled off after 6 mg mL^{-1}, and the highest scavenging rate was maintained at about 80%.Ge-CDs also

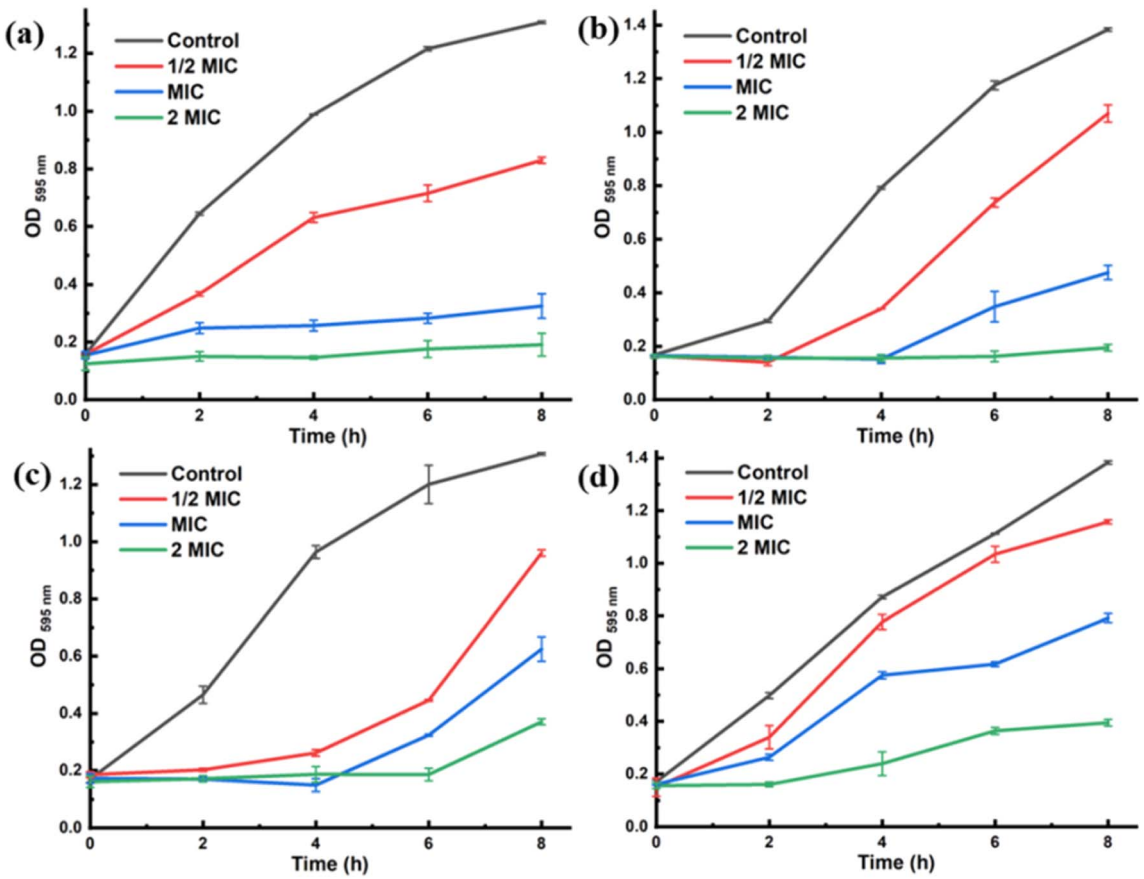

Fig. 10 Growth curve of Pk-CDs at different concentrations co-cultured with (a) *E. coli*, (b) *P. aeruginosa*, (c) *S. aureus* and (d) *B. cereus*.

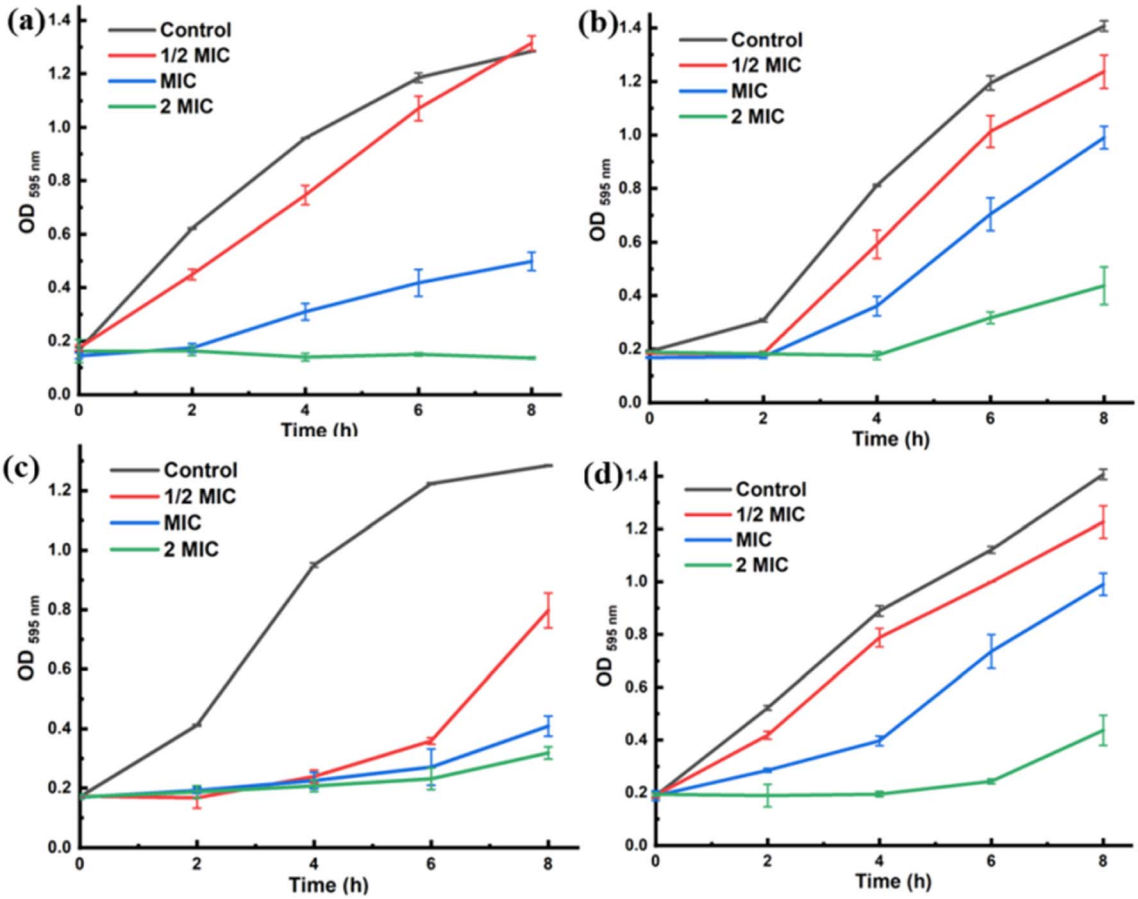

Fig. 11 Growth curve of Ge-CDs at different concentrations co-cultured with (a) *E. coli*, (b) *P. aeruginosa*, (c) *S. aureus* and (d) *B. cereus*.

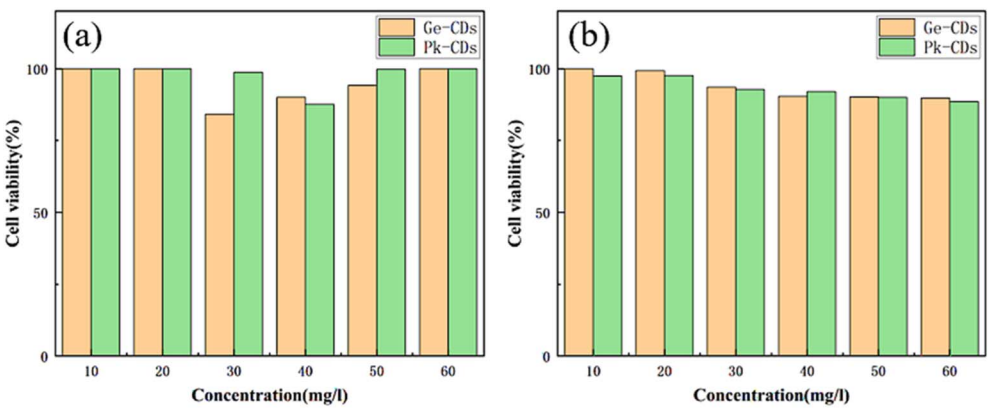

Fig. 12 Cell viability on HeLa and HaCaT cells. (a) Ge-CDs and Pk-CDs on HeLa cells, (b) Ge-CDs and Pk-CDs on HaCaT cells.

showed some DPPH radical scavenging ability, but it was weaker than that of Pk-CDs, probably due to the fact that Pk-CDs had the most –OH on the surface, and the dehydrogenation of –OH was provided to DPPH to form DPPH-H.

The NADH-PMS-NBT system was used to determine the superoxide scavenging activity of the two TCM-CDs, and the results showed that both TCM-CDs had high superoxide anion radical scavenging capacity, and the scavenging rate of both increased significantly with the increase in concentration, indicating that there was a significant quantitative relationship between their concentration and the scavenging capacity from superoxide anion radicals. Pk-CDs and Ge-CDs had IC_{50} values of 0.30 mg mL^{-1} and 0.18 mg mL^{-1}, respectively, while L-AA had an IC_{50} value of 1.731 mg mL^{-1} for the scavenging rate of superoxide anion radicals, which showed that both TCM-CDs had a much greater scavenging capacity than L-anticyclic acid

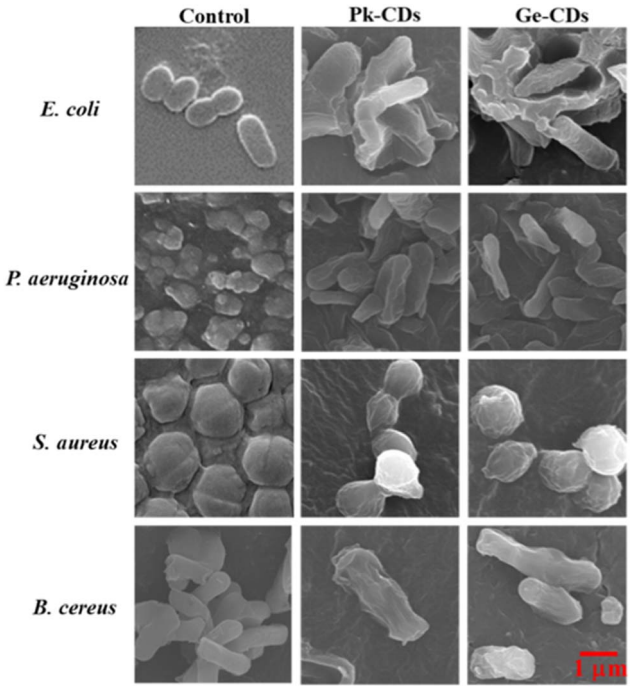

Fig. 13 The SEM image.

for superoxide anion radicals, and all had similar scavenging rates. Both of them showed a rapid increasing trend in 0.2–0.4 mg mL^{-1}, and then the slope of the curves gradually became smaller and stabilized after 1.0 mg mL^{-1}. When the concentration was 1.0 mg mL^{-1}, the scavenging rate of superoxide anion radicals by Pk-CDs, Ge-CDs was 89.2% and 83.3%, respectively, while that of L-AA was 14.0%.

The results of the hydroxyl radical scavenging ability of TCM-CDs are shown in Fig. 17; neither showed strong hydroxyl radical scavenging ability, and neither scavenged more than 20% of hydroxyl radicals in the concentration range measured.

The total reducing ability of the two TCM-CDs was determined by the potassium ferricyanide reduction method, and the color of the reaction solution gradually changed from yellow to blue-green as the concentration of the two TCM-CDs increased, and its absorbance value at 700 nm increased with the increase in concentration. The concentrations of the two TCM-CDs and their total reducing capacities showed an obvious quantitative-effect relationship, and the reducing capacities of the two TCM-CDs gradually increased with the increase in concentration.

The total antioxidant capacity of the two TCM-CDs was determined by phosphomolybdenum complex method, and it was found that both TCM-CDs had total antioxidant capacity, and their total antioxidant capacity increased with increasing concentration, indicating that they both had a quantitative relationship.

The chelation rate of Fe^{2+} by the two TCM-CDs was very limited, and the increase in chelation rate with increasing concentration was very small, and the chelation rate was less than 40% at concentrations up to 10 mg mL^{-1} (Fig. 15, Table 4).

3.3.2 *In vivo* antioxidant activity

3.3.2.1 Changes in mouse morphological characteristics. After 30 days of feeding mice according to the experimental design, observations showed that all groups except the blank control group exhibited varying degrees of weight loss, slowed movement, yellowed and dull fur, reduced resistance to capture, and significant aging features after day 30. The model group showed the most severe symptoms compared to other groups, indicating that all experimental groups, except the blank group, exhibited oxidative damage and aging symptoms, confirming the successful modeling.

3.3.2.2 Changes in mouse body weight. After 30 days of treatment, the weight gain of the Model group (MG) and NG mice was 5.35 g and 2.02 g, respectively. Weight gain in the MG group was significantly lower ($p < 0.01$), indicating successful induction of aging model mice for evaluating the anti-aging effects of TCM-CDs. Both TCM-CDs showed a dose-effect relationship in enhancing mouse weight. Compared to the MG group, the weight gain in the Pk-CDs-LD, Pk-CDs-MD, and Ge-CDs-HD groups was 4.07 g, 4.50 g, and 4.27 g, respectively, significantly increasing mouse weight ($p < 0.05$); the weight gain of Pk-CDs-HD was 5.78 g, significantly increasing mouse weight ($p < 0.01$) (Table 5).

3.3.2.3 Effects of TCM-CDs on biochemical parameters in mice. The SOD activity levels in the plasma and tissues (liver, heart, and kidneys) of the mice are shown in (Fig. 16), The SOD enzyme activities of mice in the MG (153.17 units per milliliter (U mL^{-1}), 42.41 U per mg prot, 53.17 U per mg prot, 53.72 U per mg prot) were all correspondingly very significantly lower than those in the NG group (222.32 U mL^{-1}, 93.71 U per mg prot, 97.27 U per mg prot, 109.66 U per mg prot) ($p < 0.01$), indicating successful modeling. The high-dose TCM-CDs groups showed significantly higher SOD activity in the plasma, liver, heart, and kidneys ($p < 0.01$). The medium-dose TCM-CDs groups also showed significantly higher SOD activity ($p < 0.05$), while the low-dose groups did not show significant differences ($p > 0.01$).

The GSH-Px activity levels in plasma and tissues (liver, heart, and kidneys) are illustrated in Fig. 17. NG group mice showed the highest GSH-Px activity (241.10 U mL^{-1}, 223.96 U per mg protein, 115.67 U per mg protein, 124.58 U per mg protein), while MG group had significantly lower GSH-Px activity (162.88 U mL^{-1}, 149.57 U per mg protein, 64.20 U per mg protein, 91.69 U per mg protein), indicating successful modeling. High-dose TCM-CDs group mice exhibited significantly higher GSH-Px activity ($p < 0.01$), similar to the positive control group (PG), and in some cases, slightly lower but not significantly different from the PG. Medium-dose TCM-CDs groups also showed significantly higher GSH-Px activity ($p < 0.01$), while low-dose groups did not show significant differences ($p > 0.05$) compared to MG.

MDA content in plasma and tissues (heart, liver, kidneys) is compared in Fig. 18. MG group had significantly higher MDA content (13.26 nmol mL^{-1}, 9.24 nmol mol^{-1} protein, 12.52 nmol mol^{-1} protein, 9.54 nmol mol^{-1} protein) compared to the control group (7.59 nmol mL^{-1}, 4.86 nmol mol^{-1} protein, 8.99

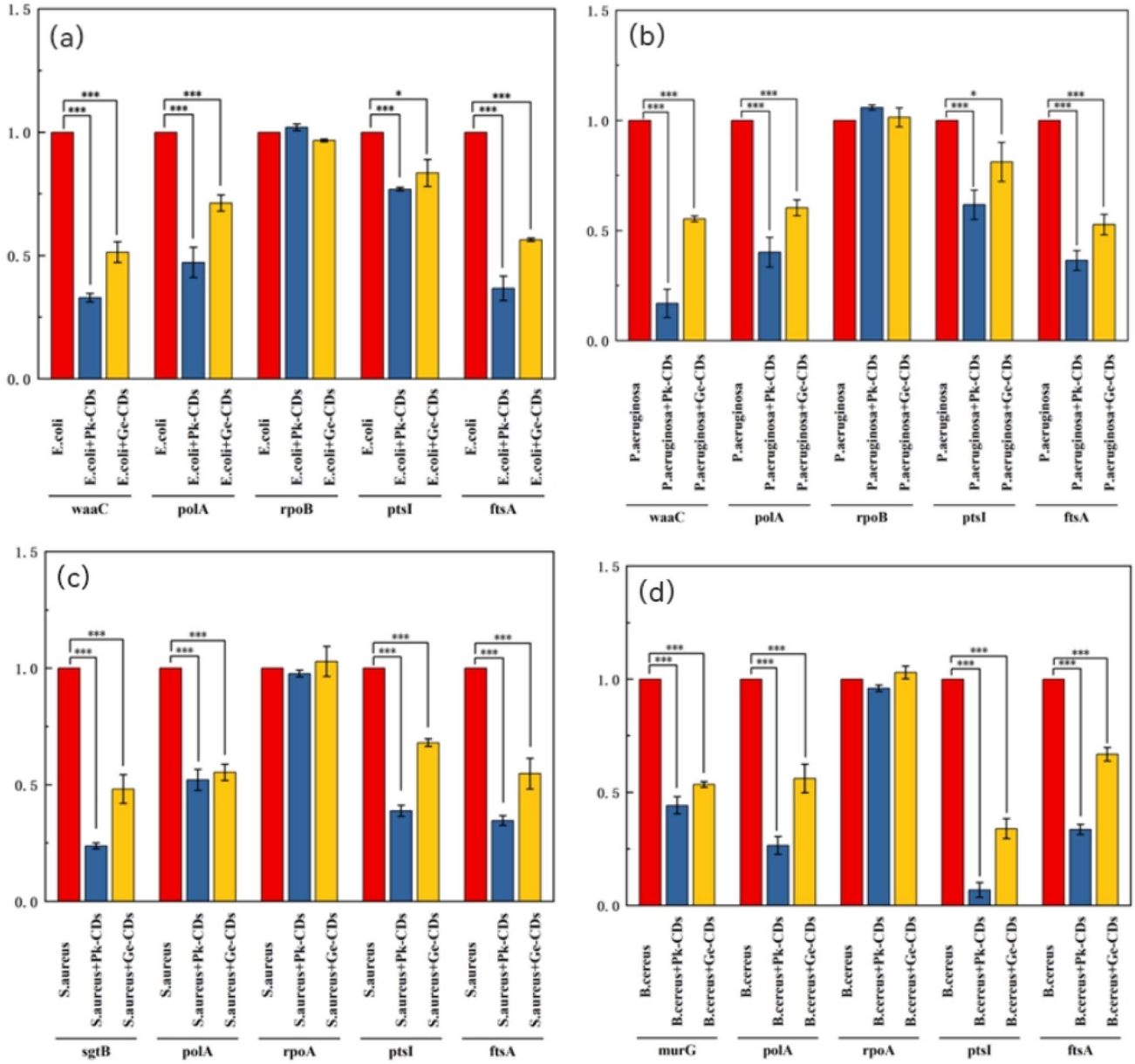

Fig. 14 Gene expression of (a) *E. coli*, (b) *P. aeruginosa*, (c) *S. aureus* and (d) *B. cereus* after treatment with two TCM-CDs (*$p < 0.05$, **$p < 0.01$, ***$p < 0.001$).

nmol mol^{-1} protein, 3.82 nmol mol^{-1} protein) ($p < 0.01$), showcasing successful modeling. PG and high-dose TCM-CDs groups showed significantly lower MDA content in plasma and tissues compared to the MG group ($p < 0.01$). Medium-dose TCM-CDs groups also demonstrated significantly lower MDA activity in plasma and heart and liver tissues ($p < 0.01$), but there was no significant difference in renal MDA activity ($p > 0.05$). Low-dose groups did not differ significantly from MG in plasma, liver, heart, and kidney MDA activity ($p > 0.05$).

3.4 Biofilm inhibition by Ge-CDs and Pk-CDs

Both Ge-CDs and Pk-CDs were evaluated for their inhibitory effects on biofilm formation by *Pseudomonas* sp. strain *41-22* and *E. coli*. The results demonstrated significant biofilm suppression by both CDs against Gram-positive and Gram-negative bacteria. A concentration-dependent decrease in biofilm biomass was observed, indicating enhanced inhibition at higher concentrations. These results suggest that Ge-CDs and Pk-CDs possess effective antibacterial activity, with biofilm inhibition trends aligning closely with their antimicrobial profiles (Fig. 19).

4. Discussion

The morphology, particle size distribution, interplanar spacing, elemental composition, and surface functional groups of Pk-CDs and Ge-CDs were thoroughly characterized using TEM, SEM, XPS, and FTIR analyses.

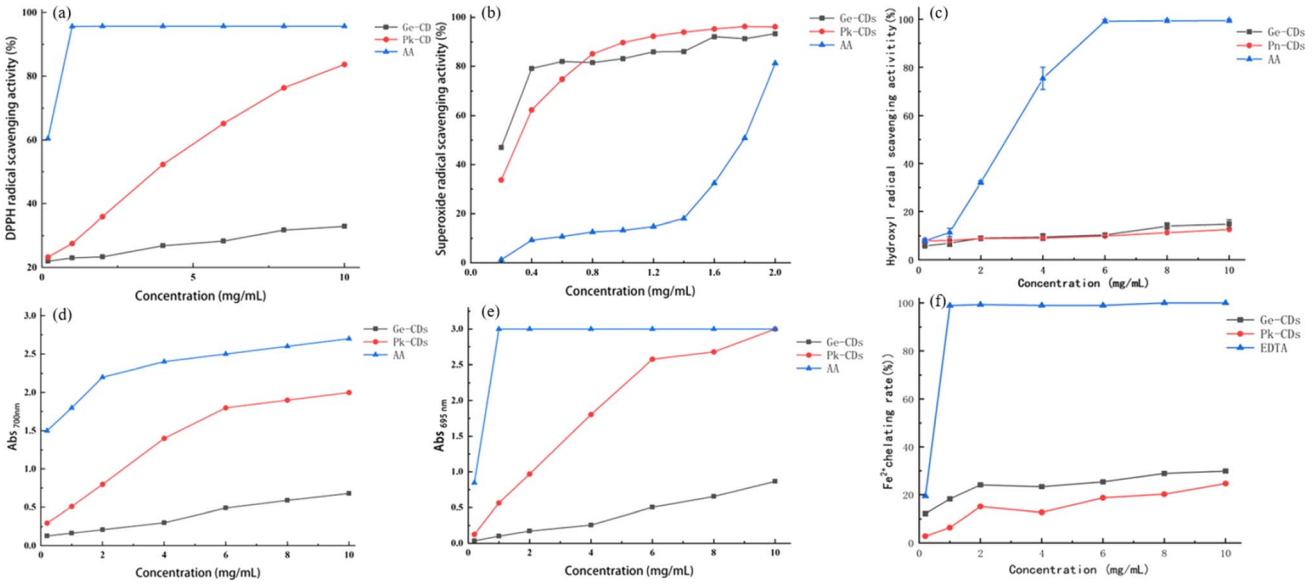

Fig. 15 Scavenging ability of two TCM-CDs to (a) DPPH radical, (b) superoxide anion radical and (c) hydroxyl radical, and (d) total antioxidant capacity, (e) total reducing force and (f) metal ion chelating power.

Table 4 IC_{50} (mg mL^{-1}) of antioxidant activity of two kinds of TCM-CDs *in vitro*[a]

IC_{50} (mg mL^{-1})	Ge-CDs	Pk-CDs	L-AA
DPPH free radical	14.33	2.994	0.1314
Superoxide anion	0.1810	0.3002	1.731
Hydroxyl radical	47.99	55.70	1.858
Sequestration	15.79	25.09	0.2882

[a] IC = inhibitory concentration, Pk-CDs = *Polygonatum kingianum*-carbon dots, Ge-CDs = *Gastrodia elata*-carbon dots, L-AA = L-ascorbic acid.

Table 5 Weight changes of mice before and after lavaging[a]

Group	Initial weight (g)	Final weight (g)	Increment
NG	20.01 ± 0.85	25.36 ± 1.40	5.35 ± 1.82
MG	20.13 ± 1.40	22.15 ± 1.59	2.02 ± 1.27[a]
PG	20.07 ± 0.96	24.77 ± 1.00	4.70 ± 1.37[c]
Pk-CDs-LD	19.07 ± 1.35	23.13 ± 0.94	4.07 ± 1.38[b]
Pk-CDs-MD	20.96 ± 1.7	25.45 ± 1.41	4.50 ± 2.02[b]
Pk-CDs-HD	19.5 ± 1.33	25.28 ± 1.61	5.78 ± 2.27[c]
Ge-CDs-LD	19.97 ± 2.06	23.38 ± 1.23	3.42 ± 1.43
Ge-CDs-MD	18.9 ± 0.39	22.52 ± 0.88	3.50 ± 0.93
Ge-CDs-HD	19.52 ± 0.49	23.78 ± 0.89	4.27 ± 1.05[b]

[a] Compared with the NG group, group a showed a significant difference ($p < 0.01$); compared with MG, b is less than 0.05, and compared with MG, c is less than 0.01. MG = Model group, PG = positive control group. Pk-CDs-LD = *Polygonatum kingianum* – carbon dots – low dose, Pk-CDs-MD = *Polygonatum kingianum* – carbon dots – middle dose, Pk-CDs-HD = *Polygonatum kingianum* – carbon dots – high dose, Ge-CDs-LD = *Gastrodia elata*-carbon dots-low dose, Ge-CDs-MD = *Gastrodia elata*-carbon dots-middle dose, Ge-CDs-HD = *Gastrodia elata*-carbon dots-high dose.

TEM results revealed that both types of CDs were nearly spherical and well-dispersed, with no visible aggregation. The particle sizzes ranged from 3 to 10 nm, with average diameters

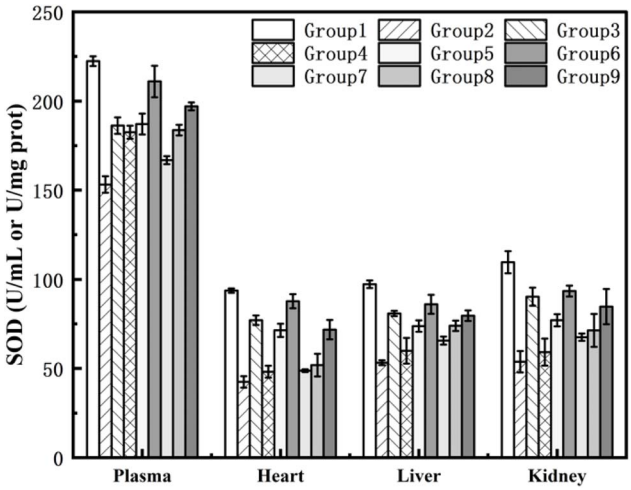

Fig. 16 SOD activity levels in mouse plasma and tissues (liver, heart, and kidney).

of 6.2 ± 0.3 nm for Pk-CDs and 6.8 ± 0.4 nm for Ge-CDs. High-resolution TEM images further showed an interplanar spacing of approximately 0.21 nm, consistent with graphitic carbon domains. These results align with previously reported nitrogen-doped carbon dos synthesized *via* pyrolysis of citric acid, typically in the range of 4–7 nm.[30] SEM imaging was employed to complement TEM by evaluating the surface morphology and aggregation behavior of the CDs on the substrate. Although individual nanoparticles of ~6 nm are below the resolution limite of conventional SEM, the images confirmed uniform dispersion without large-scale aggregation, supporting the findings observed under TEM. No significant morphological transformations were noted, as expected for particles of this scale.

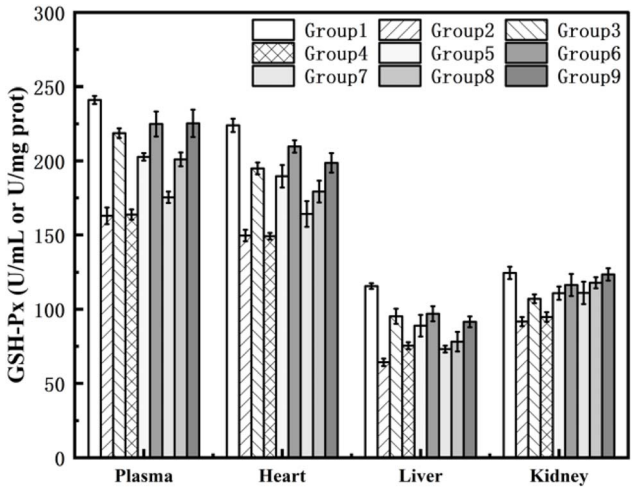

Fig. 17 GSH Px activity levels in plasma and tissues (liver, heart, and kidney).

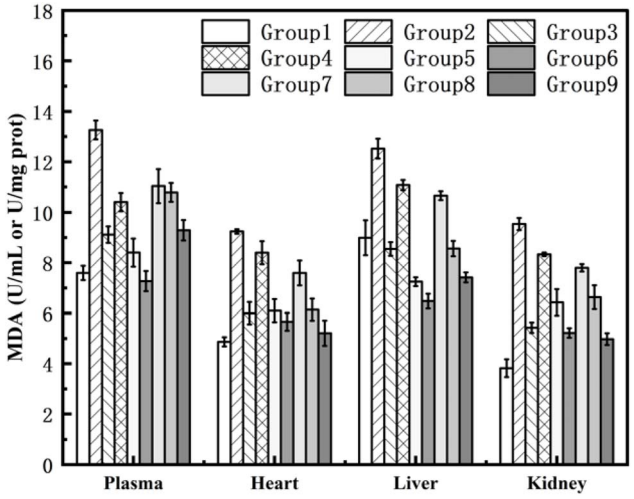

Fig. 18 MDA content in plasma and tissues (heart, liver, kidney).

The XPS spectroscopy results indicate the enrichment of the functional groups such as amino, carboxyl, hydroxyl, and carbonyl groups, which are well dispersed in solution. These functional groups not only endowed the carbon dots with good water solubility, but also enhanced the electrostatic interactions with bacterial membranes through surface charge modulation (*e.g.*, protonated amino groups), thus laying a structural foundation for the antibacterial activity.

Both Pk-CDs and Ge-CDs have good fluorescence properties attributed to π–π^* transitions and nitrogen doping effects in the sp^2 hybridized carbon structures. These findings are consistent with previous studies of herb-derived carbon dots.[4] Notably, the fluorescent properties of these CDs suggest potential applications in bioimaging, complementing their therapeutic functionality.

The Oxford cup assay demonstrated the inhibitory effect of both TCM-CDs on Gram-negative and Gram-positive bacteria. In particular, both showed optimal inhibition against the Gram-positive bacterium *Bacillus cereus*. SEM observation of bacterial morphology showed that the cell membranes of bacteria co-cultured with TCM-CDs were damaged, a phenomenon that may be attributed to the disruption of the biofilm structure by the binding of TCM-CDs to the bacterium, which resulted in a better inhibitory effect.

Lipopolysaccharide (LPS), often referred to as endotoxin, is an essential component of the outer membrane of most Gram-negative bacteria. LPS consists of hydrophobic Kdo2-lipid A and hydrophilic polysaccharide chains that play a key role in maintaining membrane permeability and structural integrity. waaC gene is a key regulator of LPS biosynthesis, and is therefore essential for membrane formation in Gram-negative bacteria. Similarly, in Gram-positive bacteria, where peptidoglycan serves as a major structural component of the cell wall, the sgtB gene is closely related to the synthesis of peptidoglycan glycosyltransferases and thus plays a key role in cell wall assembly. Our experimental results demonstrated that both waaC gene and sgtB gene expression were significantly reduced, demonstrating that these carbon dots disrupt bacterial membrane synthesis in both Gram-negative and Gram-positive strains, thereby compromising their structural integrity and metabolic functions. And the results demonstrated no significant effect on the rpoA and rpoB genes, suggesting that the antimicrobial activity of TCM-CDs mainly targets structural and metabolic processes rather than interfering with the flow of genetic information. This specificity highlights the potential of these nanomaterials as sophisticated antibacterial agents that is capable of disrupt bacterial viability without inducing extensive genetic dysregulation.

In antioxidant experiments, the antioxidant capacity of TCM-CDs was investigated by *in vitro* determination of DPPH radicals, superoxide anion radicals and hydroxyl radical scavenging assays. The results showed that the two carbon dots had significant scavenging abilities for DPPH and superoxide anion radicals, while the scavenging effect on hydroxyl radicals was weak, and this difference was related to the difference in reduction potentials of their surface functional groups. For example, phenolic hydroxyl and quinone structures are more susceptible to single-electron transfer with DPPH radicals, whereas the high reactivity of hydroxyl radicals may require the involvement of stronger electron-donating groups.[31] In addition, the limited metal ion chelating capacity of the carbon dots suggests that their antioxidant mechanism relies mainly on direct radical scavenging effects. This finding is consistent with previous studies that the antioxidant activity of carbon dots is closely related to the type of functional groups on their surfaces,[32] providing an important reference for subsequent functional optimization.

The *in vivo* antioxidant capacity of the two TCM-CDs was investigated by establishing a mouse model of oxidative damage aging, setting up low, medium and high dose groups of the two TCM-CDs for gavage of mice with oxidative loss due to D-galactose (D-gal), respectively, and finally, measuring serum, heart, liver, and spleen SOD, GSH-Px, and MDA. The experiments demonstrated that, compared with the aging model

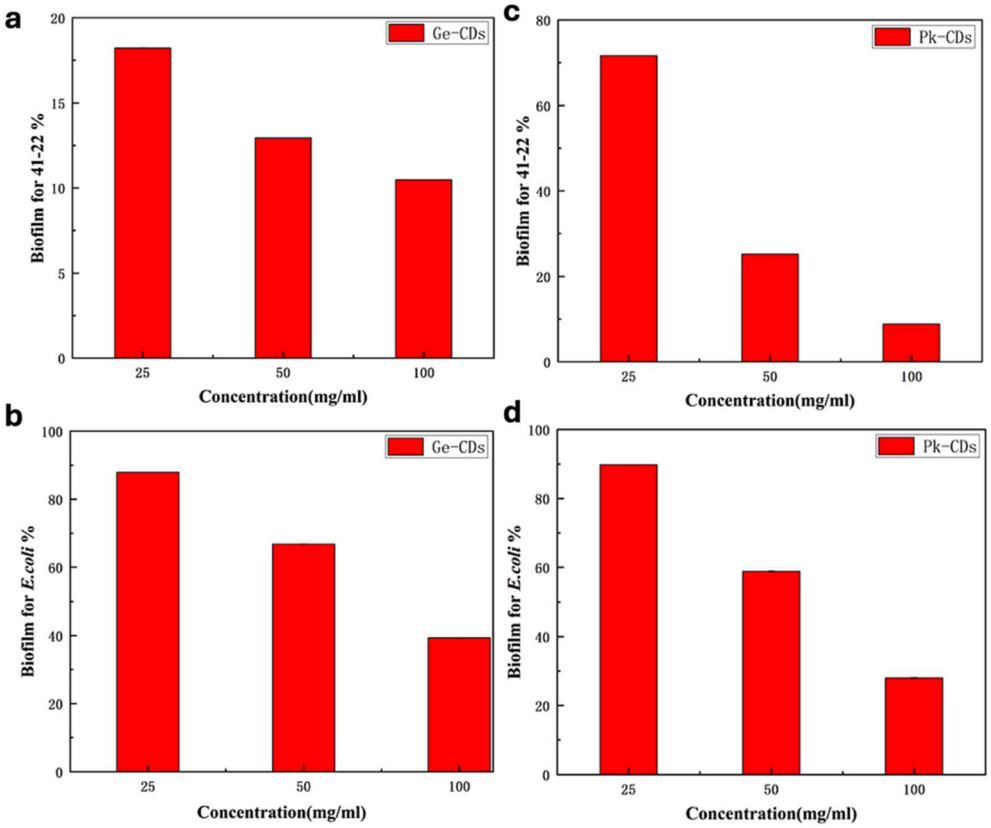

Fig. 19 Biofilm inhibitions by Ge-CDs and Pk-CDs. (a) Ge-CDs' inhibition on *41-22* and (b) *E. coli;* (c) Pk-CDs' inhibition on *41-22* and (d) *E. coli*.

group. The experiments showed that the high dose group (HD, 400 mg per kg bw per d) of the two Chinese medicinal herbs significantly increased the body weight of the mice ($p < 0.05$), significantly increased the superoxide dismutase (SOD) and glutathione peroxidase (GSH-Px) in the serum and the heart, liver, and spleen ($p < 0.05$), and also significantly decreased the serum and the malondialdehyde (MDA) levels in the heart, liver, and spleen ($p < 0.05$). levels ($p < 0.05$), suggesting that both herbal carbon dots have strong antioxidant capacity in mice and can alleviate oxidative stress by activating the endogenous antioxidant system.

There are still some limitations in this study: (1) the preparation process of carbon dots has not been fully standardized, which may lead to performance fluctuations between batches, which is a critical issue that needs to be addressed in large-scale applications. (2) The *in vivo* mouse experiments only used the D-galactose-induced oxidative damage model in mice, failing to cover other disease models (*e.g.*, inflammation or infection models), limiting the generalizability of the findings. (3) There is a lack of systematic assessment of the long-term toxicity and metabolic pathways of carbon dots, which is critical for their clinical translation. (4) Insufficient exploration of the conformational relationship between surface functional groups and biological activities of CDs, failing to further validate the roles of specific functional groups by means of chemical modifications and other means. Based on the findings and limitations of this study, future work can be carried out in the following directions: first, optimize the preparation process of CDs, and improve the homogeneity and stability of the products by controlling the reaction conditions and purification methods; second, expand the application of carbon dots in more disease models, and explore the potential of carbon dots in the field of chronic wound healing or antiaging; third, conduct in-depth studies on the *in vivo* metabolic processes and biodistribution of CDs to provide safety data for their clinical applications; and third, conduct in-depth studies on the *in vivo* metabolic processes and biodistribution of carbon dots. Third, in-depth study of the *in vivo* metabolic process and biodistribution of carbon dots to provide safety data for their clinical applications; finally, precise regulation of the functional group composition of carbon dots by means of surface modification or heteroatom doping to further enhance their biological activity and targeting.

In summary, by preparing Chinese medicine into Chinese medicine carbon dots can increase the solubility of Chinese medicine, and will not make it lose its original pharmacological activity, so as to increase the dissolution of active ingredients and further improve its biological activity, thus improving the level of efficacy of Chinese medicine. This study provides a new method to reduce the particle size and improve the clinical absorption rate of traditional Chinese medicines, and also broadens the application scope of traditional Chinese medicines, and CDs with inherent bioactivity are expected to be used in both clinical diagnosis and disease treatment in the future.

5. Conclusion and future directions

In summary, we developed CDs derived from Pk and Ge using a one-step hydrothermal method and demonstrated their multifunctional bioactivities. Both Pk-CDs and Ge-CDs exhibited uniform spherical morphology, excitation-dependent fluorescence, and excellent water solubility. The CDs showed broad-spectrum antibacterial activity against both Gram-positive and Gram-negative strains, with notable efficacy. Antioxidant assessments revealed superior radical scavenging performance by Pk-CDs, corroborated by *in vivo* evidence of reduced oxidative stress markers in a D-galactose-induced mouse model. These findings highlight the potential of plant-derived CDs as sustainable, biocompatible nanomaterials for antibacterial and antioxidant applications, and lay the groundwork for their further development in biomedical contexts.

Ethical statement

All animal procedures were conducted in strict compliance with the National Institutes of Health Guide for the Care and Use of Laboratory Animals and were approved by the Institutional Animal Care and Use Committee (IACUC) of Yunnan Minzu University. The study adhered to the "3 Rs" principles (Replacement, Reduction, and Refinement) to minimize animal use and suffering.

Data availability

The data that support the findings of this study are available from the corresponding author upon reasonable request.

Author contributions

Huili Tao: writing-review and edition. Shengting Zhang: methodology, investigation, visualization. Xiaodan Zheng: formal analysis. Sha Zhao: data curation. Yunlin Wei: supervision.

Conflicts of interest

There are no conflicts to declare.

Acknowledgements

This work was financially supported by the Yunnan Provincial Department of Education Science Research Fund Project (2024J0546) and the Yunnan Province Science and Technology Plan Project (202201AU070003).

References

1 B. Geng, J. Hu, Y. Li, *et al.*, Near-infrared phosphorescent carbon dots for sonodynamic precision tumor therapy, *Nat. Commun.*, 2022, **13**(1), 5735.
2 L. Cui, X. Ren, M. Sun, *et al.*, Carbon Dots: Synthesis, Properties and Applications, *Nanomaterials*, 2021, **11**(12), 3419.
3 A. T. Krasley, E. Li, J. M. Galeana, *et al.*, Carbon Nanomaterial Fluorescent Probes and Their Biological Applications, *Chem. Rev.*, 2024, **124**(6), 3085–3185.
4 W. K. Luo, L. L. Zhang, Z. Y. Yang, *et al.*, Herbal medicine derived carbon dots: synthesis and applications in therapeutics, bioimaging and sensing, *J. Nanobiotechnol.*, 2021, **19**(1), 320.
5 Z. A. Qureshi, H. Dabash, D. Ponnamma, *et al.*, Carbon dots as versatile nanomaterials in sensing and imaging: Efficiency and beyond, *Heliyon*, 2024, **10**(11), e31634.
6 A. Nair, J. T. Haponiuk, S. Thomas, *et al.*, Natural carbon-based quantum dots and their applications in drug delivery: a review, *Biomed. Pharmacother.*, 2020, **132**, 110834.
7 R. Atchudan, T. Edison, K. R. Aseer, *et al.*, Hydrothermal conversion of *Magnolia liliiflora* into nitrogen-doped carbon dots as an effective turn-off fluorescence sensing, multi-colour cell imaging and fluorescent ink, *Colloids Surf., B*, 2018, **169**, 321–328.
8 S. Bhatt, M. Bhatt, A. Kumar, *et al.*, Green route for synthesis of multifunctional fluorescent carbon dots from Tulsi leaves and its application as Cr(VI) sensors, bio-imaging and patterning agents, *Colloids Surf., B*, 2018, **167**, 126–133.
9 A. Deb, A. Konwar and D. Chowdhury, pH-Responsive Hybrid Jute Carbon Dot-Cotton Patch, *ACS Sustain. Chem. Eng.*, 2020, **8**(19), 7394–7402.
10 Y. Shao, C. Zhu, Z. Fu, *et al.*, Green synthesis of multifunctional fluorescent carbon dots from mulberry leaves (*Morus alba* L.) residues for simultaneous intracellular imaging and drug delivery, *J. Nanopart. Res.*, 2020, **22**, 229.
11 H. Diao, T. Li, R. Zhang, *et al.*, Facile and green synthesis of fluorescent carbon dots with tunable emission for sensors and cells imaging, *Spectrochim. Acta, Part A*, 2018, **200**, 226–234.
12 J. Kong, Y. Wei, F. Zhou, *et al.*, Carbon Quantum Dots: Properties, Preparation, and Applications, *Molecules*, 2024, **29**(9), DOI: 10.3390/molecules29092002.
13 Q. Gan, X. Wang, M. Cao, *et al.*, NF-κB and AMPK-Nrf2 pathways support the protective effect of polysaccharides from *Polygonatum cyrtonema* Hua in lipopolysaccharide-induced acute lung injury, *J. Ethnopharmacol.*, 2022, **291**, 115153.
14 X. Zhang, L. Ni, S. Hu, *et al.*, *Polygonatum sibiricum* ameliorated cognitive impairment of naturally aging rats through BDNF-TrkB signaling pathway, *J. Food Biochem.*, 2022, **46**(12), e14510.
15 Z. Chen, J. Liu, X. Kong, *et al.*, Characterization and Immunological Activities of Polysaccharides from *Polygonatum sibiricum*, *Biol. Pharm. Bull.*, 2020, **43**(6), 959–967.
16 G. Shu, D. Xu, J. Zhao, *et al.*, Protective effect of *Polygonatum sibiricum* polysaccharide on cyclophosphamide-induced immunosuppression in chickens, *Res. Vet. Sci.*, 2021, **135**, 96–105.
17 L. Chen, X. Liu, H. Wang, *et al.*, Gastrodin Attenuates Pentylenetetrazole-Induced Seizures by Modulating the

Mitogen-Activated Protein Kinase-Associated Inflammatory Responses in Mice, *Neurosci. Bull.*, 2017, **33**(3), 264–272.

18 M. Li and S. Qian, Gastrodin Protects Neural Progenitor Cells Against Amyloid β (1-42)-Induced Neurotoxicity and Improves Hippocampal Neurogenesis in Amyloid β (1-42)-Injected Mice, *J. Mol. Neurosci.*, 2016, **60**(1), 21–32.

19 G. Xiao, R. Tang, N. Yang, *et al.*, Review on pharmacological effects of gastrodin, *Arch. Pharmacal Res.*, 2023, **46**(9–10), 744–770.

20 M. Tuerhong, Y. Xu and X.-B. Yin, Review on Carbon Dots and Their Applications, *Chin. J. Anal. Chem.*, 2017, **45**(1), 139–150.

21 C. L. Ventola, The antibiotic resistance crisis: part 1: causes and threats, *Pharm. Ther.*, 2015, **40**(4), 277–283.

22 K. Jomova, R. Raptova, S. Y. Alomar, *et al.*, Reactive oxygen species, toxicity, oxidative stress, and antioxidants: chronic diseases and aging, *Arch. Toxicol.*, 2023, **97**(10), 2499–2574.

23 M. S. Brewer, Natural Antioxidants: Sources, Compounds, Mechanisms of Action, and Potential Applications, *Compr. Rev. Food Sci. Food Saf.*, 2011, **10**(4), 221–247.

24 K. Pyrzynska and A. Pękal, Application of free radical diphenylpicrylhydrazyl (DPPH) to estimate the antioxidant capacity of food samples, *Anal. Methods*, 2013, **5**(17), 4288–4295.

25 J. Zhang, X. Hou, H. Ahmad, *et al.*, Assessment of free radicals scavenging activity of seven natural pigments and protective effects in AAPH-challenged chicken erythrocytes, *Food Chem.*, 2014, **145**, 57–65.

26 F. Chen and G. Huang, Extraction and antioxidant activities of cushaw polysaccharide, *Int. J. Biol. Macromol.*, 2018, **120**, 1646–1649.

27 L. Jiao, B. Li, M. Wang, *et al.*, Antioxidant activities of the oligosaccharides from the roots, flowers and leaves of *Panax ginseng* C. A. Meyer, *Carbohydr. Polym.*, 2014, **106**, 293–298.

28 B.-M. Lue, N. S. Nielsen, C. Jacobsen, *et al.*, Antioxidant properties of modified rutin esters by DPPH, reducing power, iron chelation and human low density lipoprotein assays, *Food Chem.*, 2010, **123**(2), 221–230.

29 Q. Shia and Z. Jiang, Extraction and *in vitro* antioxidant activity of flavonoids from edible foxtail grass, *J. Food Biotechnol.*, 2013, **3**, 307–312.

30 Z. Zhang, S. Lu, G. Shen, *et al.*, Controllable and rapid synthesis of nitrogen-doped ordered mesoporous carbon single crystals for CO_2 capture, *J. CO2 Util.*, 2022, **56**, 101851.

31 V. Ruiz, L. Yate, I. García, *et al.*, Tuning the antioxidant activity of graphene quantum dots: protective nanomaterials against dye decoloration, *Carbon*, 2017, **116**, 366–374.

32 Z. Ji, A. Sheardy, Z. Zeng, *et al.*, Tuning the Functional Groups on Carbon Nanodots and Antioxidant Studies, *Molecules*, 2019, **24**(1), DOI: 10.3390/molecules24010152.